

# Thrust Measurements of a waveguide Electron Cyclotron Resonance Thruster

M.R. Inchingolo,<sup>1</sup> M. Merino,<sup>1</sup> M. Wijnen,<sup>2</sup> and J. Navarro-Cavallé<sup>1</sup>

<sup>1</sup>*Equipo de Propulsión Espacial y Plasmas, Universidad Carlos III de Madrid, Leganés, Spain.*

<sup>2</sup>*Ienai space, Leganés, Spain*

(\*Electronic mail: minching@pa.uc3m.es)

(Dated: 08 November 2023)

Direct thrust measurements are performed on a circular waveguide ECR thruster working at 5.8 GHz using a pendulum thrust balance with mechanically amplified displacement. Thrust levels between 1–3.5 mN are found for power levels in the range of 60–350 W and Xenon flow rate between 2 and 8 sccm. A maximum thrust efficiency of 3.5% is reached at 2 sccm and 60 W. Plasma plume diagnostics are used to estimate the thruster partial efficiencies to understand the main losses, and to perform a comparative analysis between directly and indirectly measured thrust. Results suggest that the low energy conversion efficiency and propellant utilization efficiency (<6.4% and <53%, respectively) are the key factors spoiling the ECR thruster performance. Lastly, Retarding Potential Analyzer measurements show the presence of energetic electrons with energy tail up to about 300 eV.

## I. INTRODUCTION

Electrodeless plasma thrusters<sup>1,2</sup> offer the potential for enhanced simplicity and extended operational lifetimes compared to Hall thrusters and gridded ion thrusters, which are susceptible to erosion, performance degradation, and more complex electronics. Nonetheless, current electrodeless plasma thrusters suffer the drawback of lower specific impulse  $I_{sp}$ , thrust efficiency  $\eta_F$ , and increased plume divergence when compared to these established technologies. These factors are critical parameters that must first be understood and then addressed before a successful transition from the prototype stage to their integration on a satellite can be made.

The Electron Cyclotron Resonance Thruster (ECRT)<sup>3–8</sup> is a type of electrodeless plasma thruster that relies on said resonance to couple electromagnetic power to the plasma electrons. In general, these devices consist of a cylindrical source immersed in a static, quasi-axial magnetic field. The exciting electromagnetic wave is injected into the system through a transmission line.

The resonance occurs where the electron cyclotron angular frequency  $\omega_{ce} = eB/m_e$  equals the excitation frequency  $\omega$ <sup>9,10</sup>, which is typically in the microwave (MW) range. The ECR heats up the electrons. Part of the coupled power is spent on sustaining ionization, and ideally, the remaining part should be transformed into plasma kinetic energy. The latter occurs thanks to the expansion of the plasma along the magnetic nozzle<sup>11,12</sup>, which is quasi-neutral and current-free, thus no neutralizer electrode is needed. However, a considerable fraction of power is lost on plasma-wall recombination, excitation losses, and divergence losses<sup>13,14</sup>.

Two main strategies for coupling the microwave power into the plasma have been explored, differing in the way MW is injected and propagated into the plasma chamber: the circular waveguide and the coaxial ECRTs. The first method consists of MW injected in the TE<sub>11</sub> (Transverse Electric) mode from a cylindrical waveguide through a dielectric window; the

second method instead brings MW power through a coaxial cable and relies on the presence of an additional central conductor to obtain a TEM propagation mode. The coaxial ECRT was first developed at ONERA (France), showing promising and competitive performance<sup>5–8</sup>, and raising interest in it elsewhere<sup>15,16</sup>. This design, however, is not strictly electrodeless and suffers the erosion of the central conductor and metallic deposition on the thruster backplate<sup>7</sup>, posing a limitation on lifetime.

The first studies involving waveguide-coupled ECRT concepts started in the 1960's carried out by Crimi *et al.*<sup>3,17,18</sup>. These tests were performed at 8.35 GHz of MW frequency, in the kW power range. Although several technological challenges were experienced, thrust balance (TB) measurements were performed on the Mark VA-S thruster. Both noble gases (Ar, Kr, Xe) and mercury propellant were tested, however, the measurements for noble gases were undermined by entrainment and out-gassing. The thrust efficiency for the mercury propellant was found to be less than 10%. Additionally, Crimi *et al.* found preliminary evidence of a high-energy electron population in the plume of their waveguide thruster<sup>3</sup>. In the 1990's, indirect thrust measurements were performed by Sercel<sup>4</sup> resulting in an estimated 2% thrust efficiency for a 500W class thruster working at 2.1 GHz with Argon as a propellant.

In Ref.<sup>6</sup>, Vialis *et al.* performed the first direct thrust measurements on a coaxial ECR thruster, measuring 1 mN of thrust with a thrust efficiency up to 11% (50W and 1 sccm of Xenon). In a more recent study, Peterschmitt *et al.*<sup>7</sup> performed the first comparison of thrust measurements between coaxial and waveguide-coupled ECR thrusters using Xenon as propellant. The tested waveguide thruster was designed with the same dimensions and operated at the same working point as the coaxial version (diameter  $D = 27.5$  mm, length  $L = 20$  mm), 10–50 W of deposited power at 2.45 GHz for 1 sccm of Xenon propellant mass flow rate. To allow MW propagation in a waveguide of the same diameter as the coaxial thruster, a dielectric filling was used at the MW injection point. The different plasma-wave coupling resulted in thrust

efficiencies of 5% and 1% respectively for the coaxial and waveguide thrusters. Additionally, a larger plume divergence and lower ion energy were found for the waveguide architecture. Similarly to what was found by Crimi *et al.*, high-energy electrons were observed, but only for the coaxial configuration of the device. Thus, the performance difference was partially attributed to the existence of this electron population in the coaxial thruster only: hot electrons can drive the plasma acceleration in the magnetic nozzle, and overall, affect the operation of this part of the thruster<sup>19</sup>. However, the physical mechanism producing these electrons, and their influence on the plume expansion are not yet fully understood and deserve additional research. Finally, the potential impact on the performance of the embedded dielectric used in the waveguide design was not fully addressed. In order to further investigate the physics of waveguide ECRTs and identify the limitations of this technology, in this work we report thrust and plasma plume measurements of a newly designed waveguide ECRT<sup>20–23</sup>.

The MW frequency used is 5.8 GHz, allowing for smaller waveguide dimensions ( $D = 36$  mm) with respect to the usual 2.45 GHz frequency ( $D \approx 80$  mm), and consequently lowering the size of the device, its mass flow rate and power requirements. Thanks to this design choice, no dielectric filling of the waveguide is needed as in<sup>7</sup>. This prevents altering the MW propagation and removes a potential source of losses from the device. The prototype used is based on the one introduced in<sup>22</sup>, including an updated version of the propellant injector.

In our previous work<sup>22</sup>, indirect measurements and estimations suggested thrust levels and thrust efficiency below 1 mN and 2% respectively, input MW in the range of 80 – 300 W at 1 – 4 sccm of Xenon mass flow rate. Here, the first direct thrust measurements performed on this prototype are presented. These are also the first measurements of their kind for a Xenon-operated ECR waveguide thruster in this power range. These results are complemented by and compared against electrostatic probe measurements (Langmuir Probe, Faraday Cup, and Retarding Potential Analyzer) in the plume region, which allows for assessing and discussing partial efficiencies and thus the main loss mechanisms. This study also brings attention to the limits of typical indirect thrust measurements on similar devices and how they compare with direct ones. Additionally, we report on partial evidence of the existence of suprathermal electrons in this waveguide ECRT design.

The rest of the paper is organized as follows. In section II, the ECRT, the thrust balance, the plasma probes, and their assembly in the vacuum chamber are presented; further details regarding the thrust balance calibration system and procedures are presented in the appendix A. In section III, the thrust and plume measurements are shown and discussed. Finally, section IV summarizes the conclusions of this work.

## II. EXPERIMENTAL SETUP

### A. Thruster and power transmission line description

The waveguide ECRT prototype, object of this test campaign, is shown in figure 1, and its main design parameters are listed in table I. The basic design is detailed in<sup>22</sup>, however, for the sake of completeness, and to highlight the updated parts of the setup, a brief description of the prototype is provided next.

The thruster design consists of three main components: the DC-block, the aluminum waveguide, and the plasma discharge chamber (PC). A magnetic field generator axially aligned with these, produces the magnetic field necessary for the resonance and the magnetic nozzle.

The DC-block allows for keeping the PC electrically floating with respect to the transmission line and consists simply of two aligned circular waveguides, with a 2 – 3 mm vacuum gap in between. Auxiliary Ansys HFSS simulations have shown that, in this configuration, MW power leaks below 2% are obtained for gap distances below 3 mm. At the same time, the DC-block mechanically decouples the thruster and thrust balance pendulum from the waveguide transmission line. This is essential for thrust measurements since the TB relies on displacement to measure thrust.

An aluminum waveguide connects the other side of the DC-block to the PC, both with the same inner diameter and separated by a quartz window. A high-temperature Perfluoroelastomer (FFKM) o-ring, prevents propellant leaks from the PC towards the upstream waveguide.

The connection to the mounting plate of the thrust balance is done by inserting the aluminum waveguide into an anodized aluminum cylinder (in yellow in Figure 1) and securing it with a set screw. This solution ensures that the thruster is well aligned with respect to the magnetic field generator and electrically floating with respect to the TB. The PC exit plane and center-line define the coordinate system as displayed in figure 1.

A permanent magnet assembly and an electromagnet make up the magnetic field generator. The first consists of a radially magnetized ring, made of 12 Sm-Co YXG-32 magnets glued together and enclosed in an aluminum case. Figure 2 depicts the magnetic field topology and strength generated by the permanent magnet and shows the location of the ECR surface inside the device. On the other hand, the electromagnet can be used to alter the shape of the magnetic nozzle and displace the resonance position. Although the electromagnet was kept mounted, it has not been used in this work, thus all the results shown in this paper are obtained for the magnetic field generated by the permanent magnet alone.

In our previous work<sup>22</sup>, a two-hole injector was used, but this introduced visible plasma azimuthal inhomogeneities in the plume. To reduce this effect, a multi-hole injector with 12 orifices of 1 mm diameter is used in this work. These holes are uniformly distributed in a circular ring (i.e. lateral side of the PC, 2 mm downstream from the quartz window or backplate). Behind these orifices, two concentric annular cavities separated by a perforated wall, all made of stainless steel,

help equalize the internal neutral gas pressure before being injected into the PC. The most external cavity is connected to a threaded stainless steel tube that feeds the thruster with the propellant, Xenon.

The mass flow rate is set and measured by a Bronkhorst EL-FLOW Select Xenon calibrated mass flow controller, with an accuracy of 0.1 sccm and 100 sccm full range. Previous experiments in<sup>22</sup> have shown that the thruster is able to ignite with a mass flow rate up to  $\dot{m}_p = 40$  sccm. However, the measurements reported here were only conducted at  $\dot{m}_p = 2, 4$ , and 8 sccm.

The waveguide transmission line connects the MW power amplifier (5.8 GHz Magnetron by IBF) with the ECRT. The transmission line setup was described in detail in<sup>22</sup>. A directional coupler, installed at the power amplifier outlet, in addition to a couple of power meters (Ladybug LB479A), allows measuring the forward power  $P_F$ , and the reflected power  $P_R$ . Then, the power delivered to the thruster can be estimated as  $P_T = P_F |S_{12}|^2 - P_R |S_{12}|^2$ , where  $|S_{12}| = 0.94$  is the transmission coefficient of the transmission line characterized with a vector network analyzer. The accuracy of the measurements of  $P_F$ ,  $P_R$ , and consequently  $P_T$ , depends on the value of the measured reflection coefficient  $\Gamma_L^2 = P_R / (P_F |S_{12}|^4)$  and the directivity of the directional coupler<sup>7,24</sup>. Hence, keeping the value of reflections low is fundamental for an accurate estimation of the power delivered to the thruster. Since up to 50% reflected power was seen in past experiments<sup>22</sup>, a manual three-stub tuner has been added downstream of the directional coupler. Thanks to this component, the reflection coefficient is kept below 6% at the directional coupler for all thruster operating points. Consequently, the delivered power uncertainty is below 15%.

## B. Vacuum facility and diagnostics

The vacuum chamber where the tests have been performed consists of a non-magnetic stainless-steel cylindrical vessel, 3.5 m long, 1.5 m in diameter. The chamber is equipped with the following pumps: a dry mechanical pump Leyvac LV80 with a pumping speed of about 80 m<sup>3</sup>/h, a pair of turbomolecular pumps, Leybold MAGW2.200iP with 2000 l/s of pumping speed each, and three cryo-panels, Leyvac 140 T-V. The total pumping speed is about 37,000 l/s for Xe, reaching an ultimate pressure of 10<sup>-7</sup> mbar in dry conditions. This facility allows keeping an operational pressure between  $2 \cdot 10^{-6}$  –  $8.4 \cdot 10^{-6}$  mbar for a Xenon flow of 1 to 8 sccm, with the pressure-to-gas load response being linear in this range. To prevent any potential leak of MW radiation into the laboratory, the vacuum chamber optical windows were covered with metallic meshes, and a microwave leak detector calibrated for the working frequency was constantly used to monitor the radiation level to ensure safety.

The thruster outlet section is about 2 m away from the chamber downstream wall and it is aligned with the chamber center line, aiming to minimize the plume-chamber wall interaction. As depicted in figure 1, the plasma discharge chamber and the magnetic field generator are directly attached to the

<b>Plasma Chamber Diameter</b>	36 mm
<b>Plasma Chamber Length</b>	20 mm
<b>MW frequency</b>	5.8 GHz
<b>B resonance</b>	2070 G
<b>Magnet type</b>	Sm-Co YXG-32
<b>Microwave Power</b>	60-350 W
<b>Mass flow rate (Xe)</b>	1-8sccm

TABLE I. Waveguide ECRT prototype design and operational parameters.

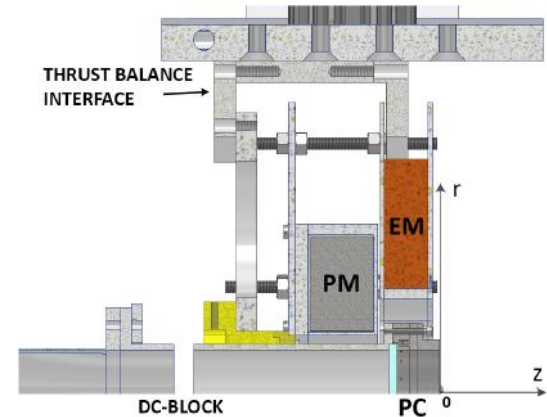


FIG. 1. Cross section of the thruster assembly, PM stands for permanent magnet, EM for electromagnet, and PC for plasma chamber. All the thruster elements (backplate holding the PC-waveguide, electromagnet, and permanent magnet) are fixed mechanically to the thrust balance mechanical interface.

TB interface. The TB used in this work is the same presented in reference<sup>25</sup>, with some upgrades regarding the calibration system (see Appendix A for further details). The TB is based on the Variable Amplitude Hanging Pendulum with Extended Range (VAHPER) design by Polzin *et al.*<sup>26</sup>. The main peculiarity of this design is that it relies on a mechanical amplification of the displacement. For the case of the TB in this analysis, the angular displacement is amplified by a factor of 31<sup>25</sup> at the sensor position. The displacement response of the TB is directly proportional to the thrust force, and the proportionality constant, which depends essentially on the mass distribution of the system (including the thruster) and stiffness of the hinges, is determined by means of calibration. In reference<sup>25</sup>, a calibration system based on a voice coil was used. The voice coil applied a calibrated force to the vertical arm, causing a controlled displacement. In the case of permanent magnet thrusters, such as the one used in this work, the force applied by the voice coil may be affected by the interaction with the permanent magnet magnetic field, which is not negligible at the voice coil location. To avoid this problem, a new calibration system based on the use of pre-calibrated weights applied to an additional horizontal arm has been implemented. This calibration system, together with the TB measurement procedure is further discussed in the appendix A. On a side note, the DC-block axis and the thrust force vector are aligned, therefore an electric force, due to the thruster discharge chamber floating potential,  $V_T$ , between the two DC-block sides would



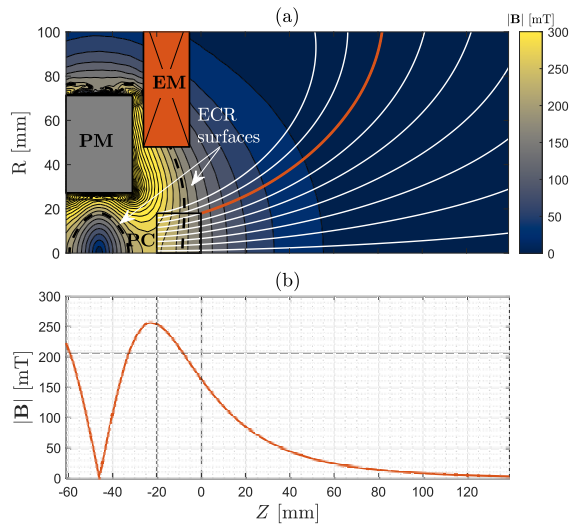


FIG. 2. (a) 2D plot of the ECRT magnetic field for zero current in the electromagnet (EM). White lines are magnetic field streamlines, and the black dashed line represents the ECR layer. The red magnetic line is the one that connects with the lip of the plasma chamber. (b) Magnitude of the on-axis magnetic field generated by the permanent magnet (PM). The horizontal line is the magnetic field magnitude that matches the ECR (2070 G for 5.8 GHz). The solid vertical line is the location of the PC backplate. The dashed vertical line is the location of the PC exit plane.

be seen as a thrust. However, this force is estimated to be in the  $\mu\text{N}$  range in the experimental conditions here described and, therefore is considered negligible. This has been confirmed by actively biasing the thruster to up to 200 V (value higher than the  $V_T$  here measured), which did not result in any appreciable displacement on the thrust balance.

In addition to the TB, intrusive electrostatic probes were used: a Retarding Potential Analyser (RPA), a Faraday Cup (FC), and a Langmuir Probe. These were mounted on a polar probe positioning system located in front of the thruster<sup>22</sup>. This system is capable of displacing the probes on a plane along the radial  $\rho$  and polar direction,  $\alpha$ . The resolution of the system is  $1^\circ$  and  $300\mu\text{m}$  for the polar and radial directions respectively. The center of rotation of the probe positioning system is aligned with the thruster exit plane.

The RPA (Impedance-Semion single button, four grids probe) was positioned at a distance of  $\rho = 350\text{ mm}$  from the thruster exit plane and used to assess the ion energy distribution function (IEDF), and ion mean energy, in the far plume. The FC measured the ion current profile and provided information on the utilization efficiency and plume divergence. The probe is equipped with an aperture diameter of  $D_{FC} = 10\text{ mm}$ . A bias of  $-120\text{ V}$  was typically used at the FC collector, a higher voltage resulted in the divergence of the collected ion current, being likely affected by either sheath expansion outside of the probe and/or secondary electron emission, increasing the effective aperture area ( $A_{FC} = \pi D_{FC}^2/4$ ). The

probe scanned the plume on a plane at constant  $\rho = 350\text{ mm}$  varying  $\alpha$  within  $-\pi/2 < \alpha < \pi/2$ . Additionally, the Langmuir probe provided supplementary information on the local electron temperature, which was used to improve the understanding and discussion of the results. Ref.<sup>27</sup> provides more information about the design and operation of the Langmuir and FC probes used in this work. Propagation of uncertainty was used to assess the measurement error for the data presented in section III. Finally, the thruster discharge chamber floating potential  $V_T$  was acquired during the overall test campaign to assess the stability of the thruster's operating point while performing thrust balance and probe measurements.

### III. RESULTS

#### A. Direct thrust measurements

Thrust measurements have been performed for three Xenon flow rates,  $\dot{m}_p = 2, 4$  and  $8\text{ sccm}$ , and power in the range  $P_T = 60 - 350\text{ W}$ . The TB described above has been used to evaluate the thrust produced by the ECRT,  $F_{TB}$ . Once thrust is measured, the specific impulse  $I_{sp}$  and thrust efficiency  $\eta_F$  can be computed as follows,

$$I_{sp} = \frac{F_{TB}}{\dot{m}_p g_0}; \quad \eta_F = \frac{F_{TB}^2}{2\dot{m}_p P_T}. \quad (1)$$

Results for  $F_{TB}$ ,  $I_{sp}$  and  $\eta_F$  are shown in figure 3. The measured thrust levels fall in the range  $F_{TB} = 1-3.5\text{ mN}$  and scale almost linearly with power at a constant Xe flow rate. The maximum thrust,  $3.5\text{ mN}$ , is reached at the working point of  $8\text{ sccm}$  and  $350\text{ W}$ . The thrust-to-power ratio,  $F_{TB}/P_T$  is also computed and lies between  $5$  and  $20\text{ mN/kW}$ , decreasing with power for  $2$  and  $8\text{ sccm}$  but staying rather constant for the case at  $4\text{ sccm}$ . Repeated measurements under the same thruster operating condition typically yielded values within  $5\%$  of the reported ones.

The highest specific impulse,  $800\text{ s}$ , was obtained at  $2\text{ sccm}$  and  $260\text{ W}$ . On the contrary, the lowest was reported for  $8\text{ sccm}$  and  $80\text{ W}$ , being only  $200\text{ s}$ . Specific impulse  $I_{sp}$  scales well with  $\sqrt{P_T/\dot{m}_p}$ . The data points in the explored range can be fitted, with an average thrust efficiency of  $\eta_F = 2.34\%$ .

The thrust efficiency  $\eta_F$  ranges in  $1-3.5\%$  in the tested cases, being lower than the ones reported by Crimi with mercury propellant<sup>3</sup> at higher power levels ( $\eta_F \approx 10\%$  at  $800\text{ W}$  and  $0.3\text{ mg/s}$ ), but not far from those obtained by Peterschmitt ( $\eta_F = 1\%$  at  $25\text{ W}$ ,  $1\text{ sccm}$  of Xenon)<sup>7</sup>.

No clear dependence on the mass flow rate and power was found for the thrust efficiency:  $\eta_F$  decreases with power for  $2\text{ sccm}$ ; it increases for  $4\text{ sccm}$ ; and remains fairly constant for  $8\text{ sccm}$ .

#### B. Electrostatic probe measurements

To understand the underlying physical mechanisms driving the observed performance, plume measurements were taken

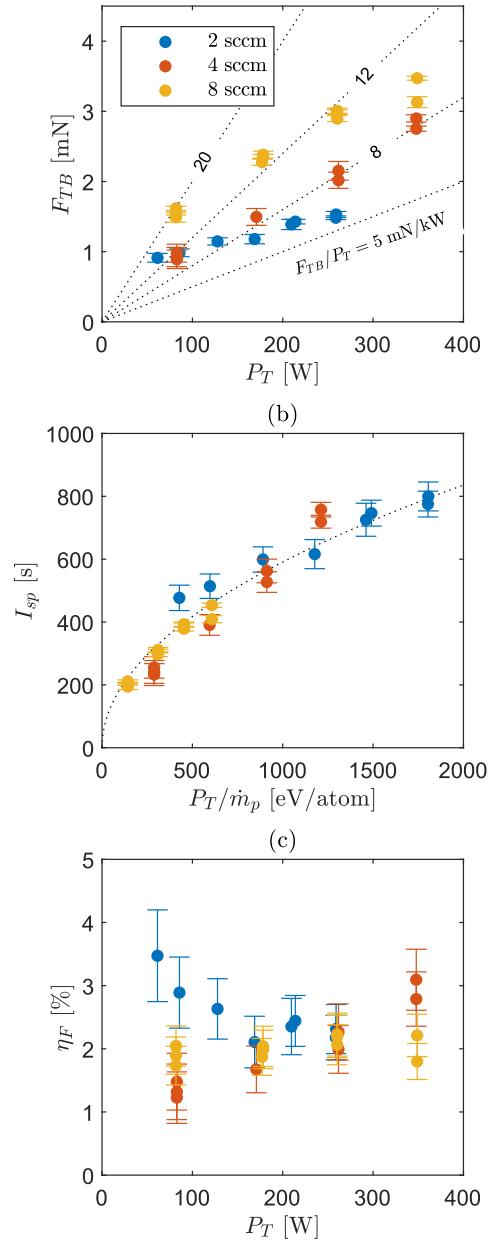


FIG. 3. Direct thrust measurement results for a set of different  $\dot{m}_p$  and power. (a) Measured thrust  $F_{TB}$ , the constant thrust-to-power ratio levels are shown as dotted lines. (b) Specific impulse  $I_{sp}$  as a function of  $P_T / \dot{m}_p$ . In the range studied, the latter scales well with  $\sqrt{P_T / \dot{m}_p}$ , the dotted curve represents the fitted  $I_{sp}$  at constant thrust efficiency  $\eta_F = 2.34\%$ . (c) Thrust efficiency  $\eta_F$ . Error bars have been obtained by the propagation of measurement uncertainties.

with electrostatic probes. The same mass flow rates as in section III A were tested (2, 4, and 8 sccm), for a subset of the power levels in figure 3. The FC ion current density as a function of the angular position,  $j_i(\alpha)$ , is shown in figure 4.  $j_i$  results from dividing the collected current by the aperture area of the probe, and is expressed as  $j_i = I_{FC} / A_{FC}$ . At 4 and 8 sccm, the increase of power leads to a larger amount of collected current at small angles, while at large azimuth angles, the power increase seems to play a little role in the collected current. At the lowest mass flow rate, 2 sccm, the effect of increasing power is unclear, a maximum on-axis current density is obtained for 130 W. In general, two qualitatively different ion current density profiles are observed, featuring a singly- or doubly-peaked plume ("hollow plume"). This structure, and also a triply-peaked plume, were observed in previous experiments<sup>22</sup>. The transition from a double peak to a single peak profile depends on the power-to-mass flow rate ratio. The threshold for the transition to the single peak is found to be about  $P_T / \dot{m}_p \gtrsim 500$  eV atom<sup>-1</sup>. Thus, for the explored cases this transition is only observed at 4 sccm, while the 2 sccm and 8 sccm cases remain at the single/double peak profile respectively. This ion current profile structure might be linked to the propellant being injected in the radial direction (i.e. from the lateral walls of the PC). Additional measurements of the electron temperature, taken 130 mm downstream from the thruster outlet by means of the Langmuir probe, confirm that the temperature on-axis of the ejected beam is lower (4 eV) than that off-axis (6 eV) at the same axial distance and  $\alpha = 40$  deg. This suggests that, for low  $P_T / \dot{m}_p$ , there could be a tendency for power to be coupled more efficiently in the vicinity of the walls (i.e. gas injection location), potentially promoting ionization there, which, in turn, might lead to the formation of this hollow plume structure. To further investigate this hypothesis and obtain clues on MW power absorption, simulations employing similar approaches to those used in Ref.<sup>14,28</sup> should be performed.

The RPA is used to extract information on the ion velocity distribution function (IVDF) in the  $\rho$  direction, as a function of the ion kinetic energy  $K_i$ :  $f(K_i)$ <sup>29,30</sup>. Assuming the presence of singly charged ions only,

$$f(K_i) \propto \partial I_c / \partial V_{G2}, \quad (2)$$

$$K_i = \frac{1}{2} m_i v_i^2 = e(V_{G2} - \phi), \quad (3)$$

where  $I_c$  is the current collected by the RPA,  $V_{G2}$  is the ion energy scanning grid bias,  $v_i$  the local ion velocity and  $\phi$  the plasma potential at the measurement location,  $m_i$  and  $e$  are the ion mass and the electron charge respectively. The resulting curve is the convolution of the actual IVDF with the probe apparatus transfer function. In the absence of information about the latter, in the rest of this study, the effects introduced by the probe apparatus are neglected and no corrections are applied to the IVDF. The ion mechanical energy,  $E_i$ , is defined as the sum of kinetic plus potential energy,  $E_i = K_i + e\phi = eV_{G2}$ . Thus, by assuming that along the expansion  $E_i$  is fully converted into kinetic energy and that the regime is collisionless, it is possible to obtain the ion energy distribution function

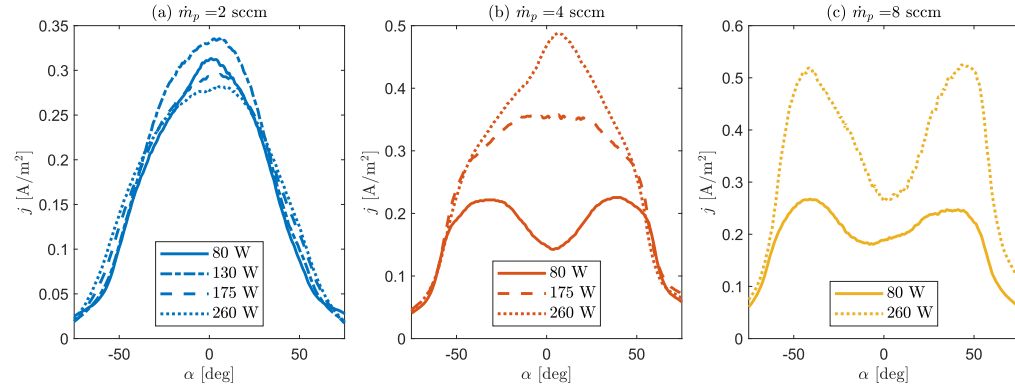


FIG. 4. Faraday Cup ion current density profiles for  $\dot{m}_p = 2$  sccm (a),  $\dot{m}_p = 4$  sccm (b) and  $\dot{m}_p = 8$  sccm (c), and various power levels. By considering the accuracy of current measurements and probe aperture diameter, the error on the measurement of  $j_i$  is estimated to be below 2%.

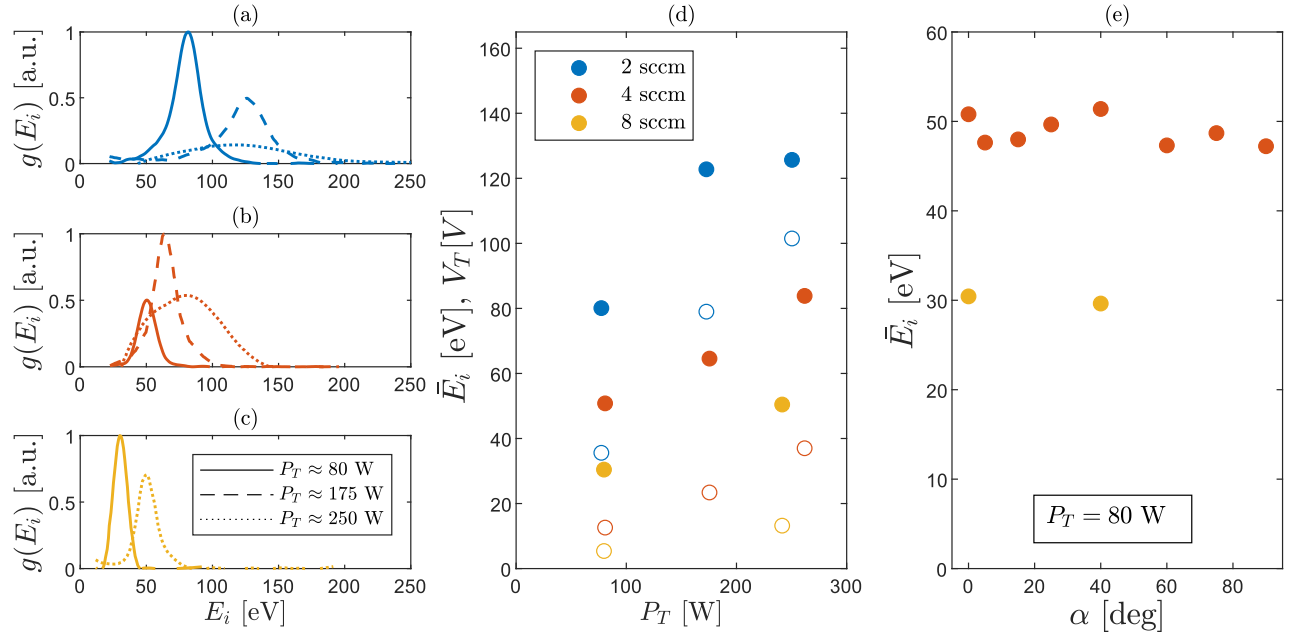


FIG. 5. Retarding Potential Analyzer (RPA) measurements. (a-c) Ion energy distribution function (IEDF) for  $\dot{m}_p = 2 - 4 - 8$  sccm (blue, red and yellow respectively). Solid, dashed, dotted lines indicate 80, 175 and 250 W respectively. (d) Mean ion energy  $\bar{E}_i$  (filled dots) based on the IEDF results, and thruster floating potential  $V_T$  (empty dots). (a-d) measurements are taken on-axis at  $\rho \equiv z = 350$  mm. Note that for the highest power case, the reflection coefficient was not constant, being  $\Gamma_L^2 = 5, 1$  and  $8\%$  for 2, 4 and 8 sccm respectively. Thus the delivered power level resulted to be  $P_T = 250, 260$  and  $240$  W. An average of 250 W is displayed in the legend. (e) Mean ion energy  $\bar{E}_i$  at different azimuth angles (same  $\rho = 350$  mm), only for 4 and 8 sccm (red and yellow) at 80 W. The uncertainty on  $\bar{E}_i$  was estimated with uncertainty propagation to be  $<5\%$  for the shown cases.

(IEDF) for  $\phi = 0$ , i.e. at the vacuum chamber walls:

$$g(E_i) = \frac{1}{\sqrt{2m_i E_i}} f(E_i). \quad (4)$$

The obtained IEDFs are shown in figure 5 for the three mass flow rates and power levels. Looking at the shape of the IEDFs (panels a-c), the increase of power at constant mass flow induces a wider spread of the ion energies. Results in agreement with these were obtained through LIF measurements

performed on this thruster in<sup>23</sup> where the spread in ion energies was referred to as axial kinetic temperature. In the present study, ion temperatures in the order of 4000 – 10000 K were found for most of the cases. This is likely the effect of a widening of the ionization region over the acceleration region, i.e. ionization might happen at different potentials, and consequently, ions would reach different axial velocities at the measurement point, which is read as a spread of the IEDF. As a result, at high  $P_i/\dot{m}_p$ , some ions can reach  $E_i > 200$  eV (2 sccm

at 250 W). Panel 5-d shows the mean ion energy  $\bar{E}_i = \langle E_i \rangle$  for the different working points. Overall, the trend is roughly linear with  $P_T/\dot{m}_p$ , which is coherent with the trend found for the specific impulse in figure 3-b with  $\sqrt{P_T/\dot{m}_p}$ . Similar trends were expected but not found by Sercel *et al.* in Ref.<sup>4</sup>, likely due to larger variations of  $\eta_F$  in the range explored in that work. The maximum here reported  $\bar{E}_i$  is about 130 eV for 250 W and 2 sccm. This panel shows as well the floating potential with respect to the ground of the metallic walls of the thruster, denoted as  $V_T$  (empty circles). Because of the wall sheath and the spatial spread of the ionization region,  $V_T$  does not equal the mean ion energy. However, it exhibits the same trend as  $\bar{E}_i$ . Hence, in the absence of IEDF measurements,  $V_T$  could be used instead as a proxy to estimate mean ion energy. Panel 5-e shows that  $\bar{E}_i$  barely depends on the azimuth angle, this observation will come in useful in section III D.

Referring to equation 3,  $v_{i\infty}$  is defined as the velocity of ions at the location where  $\phi = 0$ . The average ion velocity  $u_{i\infty} = \langle v_{i\infty} \rangle$ , ranges from 6.66 to 13.4 km/s, as obtained at the working points of 80 W, 8 sccm and 250 W, 2 sccm, respectively. It is possible to define  $\kappa_2 = \langle v_{i\infty}^2 \rangle / u_{i\infty}^2$  and  $\kappa_3 = \langle v_{i\infty}^3 \rangle / u_{i\infty}^3$  being ratios of different moments of the velocity distribution function. These parameters provide information on the dispersion of the ion velocities, and for the data presented here, they result being  $1 < \kappa_2 \leq 1.02$  and  $1.02 \leq \kappa_3 \leq 1.08$ . These will be used in Section III D.

### C. Suprathermal electrons

Previous work on ECRTs<sup>3,7</sup> has shown preliminary evidence of the existence of high-energy electrons in the plume. In both studies, electrostatic probes were used for the detection. Crimi *et al.* found such electrons in a waveguide ECRT (1-2 kW power range) by using an RPA, noting that biases up to -630 V on the primary electrons repelling grid were necessary to effectively repel all the electrons and only collect ions. On the other hand, Peterschmitt *et al.*<sup>7</sup> only found evidence of energetic electrons in their coaxial ECRT prototype but not in the waveguide version. The experiments were done by using a Faraday cup to measure the current density at different collector biases, and a bias up to -200 V was found to be necessary to repel all the electrons.

Suprathermal electrons were also found for the thruster used in this study by using an RPA. As mentioned in section II, the RPA used is composed of four grids: the external grid (G0) which is exposed to the plume, the primary electron-repelling grid (G1), the ion energy scanning grid (G2) and the secondary electron repelling grid (G3). Downstream the grids lies the collector (C).

On-axis RPA scans at different G1 biases,  $V_{G1}$ , were taken for the case at  $P_T = 175$  W and  $\dot{m}_p = 2$  sccm. The  $I_C$ - $V_{G2}$  curves resulting from the sweep of G2, are shown in figure 6-a. In the absence of electrons within the probe, negative collected currents ( $I_C < 0$ ) are representative of ion currents and should tend to zero as  $V_{G2}$  is increased and all the ions are repelled. Interestingly, for  $V_{G1} > -300$  V, and  $V_{G2}$  sufficiently large to repel all the ions,  $I_C$  is positive. This behavior

is compatible with the collection of primary electrons with enough energy to overcome the repelling electric field established by G1, effectively behaving as an additional positive constant collected current along the IV curve. Other phenomena, such as secondary electron emission from the collector surface or ionization within the probe, are also known to be possible causes of deviations from the expected IV curve of an RPA. However, both effects would be observed as an additional negative current, thus they cannot explain the observed trend.

The performed test allows for estimating the amount of electron current reaching the collector depending on  $V_{G2}$ , under the assumption that primary electrons and single ions are the only species contributing to the current collection, and the grid transparency is the same for electrons and ions. The electron to ion collected current ratio,  $I_e/I_i$  is provided in panel 6-b, where  $I_e$  is obtained from the value of the I-V curve at sufficiently large  $V_{G2}$  ( $\simeq 180$  V) and  $I_i = I_C(V_{G2} = 0) - I_e$ . The estimation of  $I_e/I_i$  has been done at four levels:  $V_{G1} = -300, -200, -100$  and  $-60$  V. In this range,  $I_i$  was found to be essentially independent of  $V_{G1}$  showing a variation of only 3.7%. Therefore, the current variation only comes from electron collection. These results suggest that electrons with an energy tail of up to 300 eV exist in the plume. At the same location and working point, an electron temperature of only  $T_e = 11.5$  eV was measured with a Langmuir probe. Hot electrons were not found at higher  $\dot{m}_p$  and/or lower power levels, suggesting that their presence and energy depend on  $P_T/\dot{m}_p$ .

These conclusions might explain the absence of these electrons for the waveguide thruster of Ref.<sup>7</sup> since a maximum  $P_T/\dot{m}_p$  of about 725 eV/atom was used in that study, about 40% lower than the one for the case shown in figure 6.

The existence of suprathermal electrons in ECR thrusters invalidates the common assumption of Maxwellian electron distribution, and further work must assess their effects on expansion physics. Numerical studies<sup>31,32</sup> have shown that, under certain circumstances, hot electrons could lead to the formation of a double layer across the plume expansion, perhaps similar to the one encountered by helicon plasma thruster experiments<sup>33</sup>. However, to the authors' knowledge, a double layer has not been observed yet in an ECRT and the origin and role of these energetic electrons in the plume expansion is not yet clear.

On the other hand, these measurements highlight the necessity for additional care when biasing electrostatic probes for magnetic nozzle ECR thrusters. This is particularly true for FCs since the collection of high-energy electrons would lead to an underestimation of the ion current density as seen by Peterschmitt in<sup>7</sup>. With the assumption that electron-to-ion current ratios similar to those shown in figure 6-b, apply when using a Faraday Cup biased at -120 V (typical value used for the cases studied), the ion current collected could be underestimated by up to about 10%.



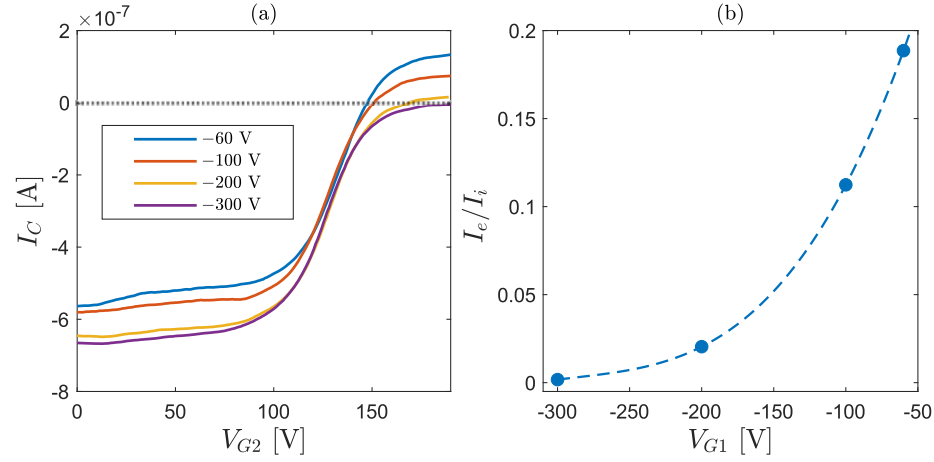


FIG. 6. (a) RPA characteristic IV curves at four different biases of the primary electron repelling grid G1 (-60, -100, -200, -300 V). (b) Ratio of the electron to ion currents collected by the RPA. (a) and (b) have been obtained for one single operating point,  $P_T = 175$  W,  $\dot{m}_p = 2$  sccm. The RPA settings for the rest of the grids and collector are: G0 is floating and used as a reference potential,  $V_{G2} = 0 - 190$  V,  $V_{G3} = V_C - 10$  V and  $V_C = V_{G1}$  V.

#### D. Assessment of partial efficiencies

Electrostatic probe measurements can be used to identify where performance losses occur by breaking down thrust efficiency into the product of several partial efficiencies, each associated with a different physical process in the operation of the device. In order to do this, certain hypotheses must be invoked. First, it is assumed that the collected ion current density consists of singly charged ions only. Second, the ion expansion is collisionless, axisymmetric, and conical from the location where the measurements are carried out ( $\rho = 350$  mm) to infinity. Additionally, it is assumed that  $\bar{E}_i(\alpha)$  does not vary much with the azimuthal angle, and therefore we take  $\bar{E}_i(\alpha) = \bar{E}_i(0)$ , which is partially supported by figure 5-e. To derive the partial efficiencies, we first introduce the integrals of different moments of the ion velocity distribution function.

The ion beam current  $I_i$  and its axial component  $I_{zi}$  are defined as:

$$I_i = 2\pi\rho^2 \int_0^{\pi/2} d\alpha \bar{j}_i(\alpha) \sin(\alpha), \quad (5)$$

$$I_{zi} = 2\pi\rho^2 \int_0^{\pi/2} d\alpha \bar{j}_i(\alpha) \cos(\alpha) \sin(\alpha), \quad (6)$$

being  $\bar{j}_i(\alpha) = 0.5 \cdot (j_i(\alpha) + j_i(-\alpha))$  the "symmetrically" averaged ion current density profile obtained from the FC measurements presented in figure 4.

The ion momentum in the z direction  $F_i(\rho)$  and beam power  $P_i(\rho)$  through a spherical surface of radius  $\rho$  around

the source are

$$F_i(\rho) = 2\pi\rho^2 \int_0^{\pi/2} d\alpha \sin\alpha m_i \int d^3v v_i v_{zi} f(v) = \frac{m_i}{e} I_{zi} u_i \kappa_2, \quad (7)$$

$$P_i(\rho) = 2\pi\rho^2 \int_0^{\pi/2} d\alpha \sin\alpha \frac{1}{2} m_i \int d^3v v_i^3 f(v) = \frac{m_i}{2e} I_i u_i^2 \kappa_3 = \frac{I_i \bar{E}_i \kappa_3}{e \kappa_2}, \quad (8)$$

where  $\kappa_2$  and  $\kappa_3$  are defined in section III B. The dependence of  $F_i$  and  $P_i$  on the radial distance is due to the ions continuing their acceleration along the potential drop in the plume. At  $\rho \rightarrow \infty$ ,  $u_i \rightarrow u_{i\infty}$  as  $\phi = 0$  and  $\kappa_2(\rho), \kappa_3(\rho) \rightarrow \kappa_2, \kappa_3$  far downstream. Consequently, we can define  $F_{i\infty}$  and  $P_{i\infty}$ .

Understanding that the largest thrust contribution in an efficient thruster is provided by the ion momentum, the thrust efficiency is approximated by:

$$\eta_F \approx \frac{F_{i\infty}^2}{2\dot{m}_p P_T} = \eta_u \eta_d \eta_e \eta_s, \quad (9)$$

where:

$$\eta_u = \frac{I_i m_i}{\dot{m}_p e}, \quad (10)$$

$$\eta_d = \left( \frac{I_{zi}}{I_i} \right)^2, \quad (11)$$

$$\eta_e = \frac{P_{i\infty}}{P_T}, \quad (12)$$

$$\eta_s = \kappa_2^2 / \kappa_3, \quad (13)$$

are the utilization, divergence, energy, and dispersion partial efficiencies, respectively. The dispersion efficiency,  $\eta_s$ , ac-



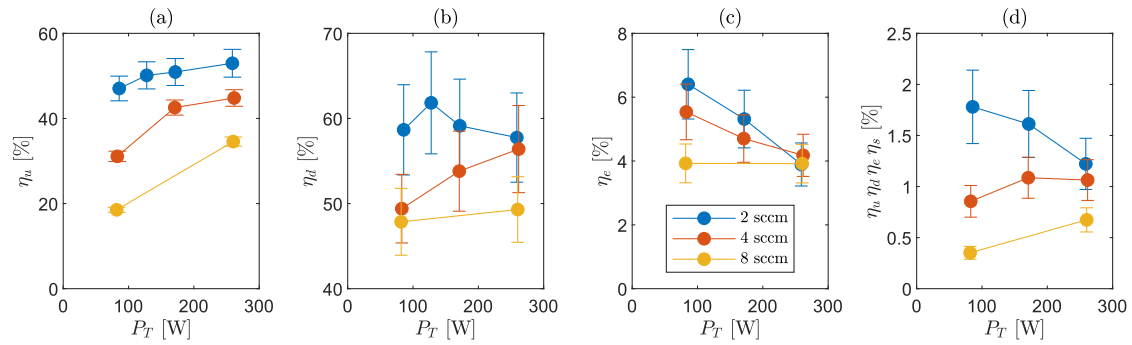


FIG. 7. Partial efficiencies  $\eta_u$ ,  $\eta_d$ ,  $\eta_e$  as a function of  $P_T$  estimated from the electrostatic probe measurements, for  $\dot{m}_p = 2 - 4 - 8$  sccm, blue, red and yellow respectively. (d) Shows the product  $\eta_u \eta_d \eta_e \eta_s$  representing an indirectly estimated thrust efficiency, as opposed to the direct measurements shown in figure 3-c.

counts for the spread in ion velocities in the radial direction  $\rho$  and has the smallest impact on the performance of the device. In fact, using the IEDFs available in figure 5, this quantity ranges between  $0.97 \leq \eta_s < 1$ .

The rest of the partial efficiencies computed according to equations 10-12 are shown in figure 7. Some general conclusions can be extracted. First, the utilization efficiency  $\eta_u$  increases roughly with  $P_T/\dot{m}_p$  within the explored range. This is expected because, with more energy per electron available, ionization collisions become more likely to occur, improving the ionization rate. Nevertheless,  $\eta_u$  seems to saturate with power, to a value that decreases with the mass flow rate. At 2 sccm, the highest  $\eta_u$  obtained is around 53%. This means that even at this relatively high  $P_T/\dot{m}_p$ , the thruster is not able to produce a well-ionized beam.

Second, the divergence efficiency  $\eta_d$  (figure 7-b) depends directly on the ion current density profile which, as already discussed, can present one or two peaks. For the 2 sccm cases, which present a single peak profile, the increase of power barely modifies the current profile shape. Thus, the divergence efficiency is almost constant at about 60 %, however, a peak of  $\eta_d$  appears at 130 W. Looking at the corresponding ion current density profiles (figure 4-a) the ion current on axis increases going from  $P_T = 80$  to 130 W, nevertheless it decreases when going to higher powers (as the current at large angles increases). A possible explanation for this trend might be associated with a larger amount of high-energy electrons collected by the FC when the power is raised, as it has been already discussed in section III C. At 8 sccm, the plume profile shows two peaks in the range studied. Since more current is found on this annular structure ("hollow plume"), this results in a lower efficiency, roughly about 48%, but almost constant with  $P_T$ . For the intermediate case at 4 sccm, the transition from double to a single peak guides the increase of  $\eta_d$  with  $P_T$ .

Third, the energy conversion efficiency  $\eta_e$  (figure 7-c) stays below 7% for all the tested operating points. Note that, by defining  $\eta_e$  as equation 12, any power deposited on the neutrals or the residual thermal energy on the electrons is neglected. This is clearly the lowest partial efficiency of those

explored in this work and points to the large losses that exist in the discharge process as the main factor spoiling the performance. Inelastic collisional losses, the loss of neutrals, the particle and power fluxes to the PC surfaces, and the microwave power radiated away from the system, all can negatively affect  $\eta_e$ . In fact, these phenomena directly impact the mean ion energy  $\bar{E}_i$  and ion current  $\bar{I}_i$ . The latter depends on the utilization efficiency,  $\eta_u$ , whereas  $\bar{E}_i$  scales with the total potential drop in the plume, which is proportional to the electron temperature. Energy losses inside the PC, mainly inelastic collisions and plasma recombination at the thruster internal walls, lower  $T_e$ . Re-ionizing the propellant that recombines at the walls further lowers the electron temperature, increasing the losses.

At 2 sccm,  $\eta_e$  drops with power, indicating that the additional power does not translate into an efficient increase of the beam power. In fact, this extra power only induces a slight increase of the ion beam current i.e. higher  $\eta_u$ , and ion mean energy  $\bar{E}_i$ , but both magnitudes seem to be saturated with input power for this case.  $I_i \cdot \bar{E}_i$  increases slower than  $P_T$ . This means that most of this extra power is diverted directly into losses. The same reasoning applies for the 4 sccm case, but  $\eta_e$  decays at a lower rate with  $P_T$ , since the relative increase of  $I_i \cdot \bar{E}_i$  is higher in the studied power range. At 8 sccm,  $\eta_e$  remains almost constant thanks to the noticeable increase of  $I_i \cdot \bar{E}_i$ , i.e.  $\eta_u$  almost doubles from 80 to 250 W, and  $\bar{E}_i$  increases a factor of 1.7 approximately. Note that MW losses are likely not affecting  $\eta_e$  negatively, since as explained in section II, those are already taken into account in the estimation of  $P_T$ . Moreover, MW radiation from the thruster and power absorption at the quartz window are assumed to be negligible. As also observed in other devices<sup>34</sup> and in simulation results<sup>13,35</sup>, it is expected that the dominant loss mechanism are losses to the lateral and rear walls, together with excitation and (re-)ionization inelastic collisions. Indeed, the LIF measurements in Ref.<sup>23</sup>, revealed a mean ion velocity of  $-500$  m/s directed towards the backplate at  $z = -10$  mm (middle of the discharge chamber) for the same thruster design as in this study.

An improved design of the magnetic field could help screen

the lateral walls and reduce wall losses (magnetic shielding). However, the backplate, which is more difficult to shield, might still be subject to large plasma losses. Additionally, an improved design of the PC/injection may reduce the loss of neutrals and help increase  $\eta_u$ . Finally, to improve the divergence efficiency, a lower-diverging magnetic field outside of the thruster may be needed. However, as seen in figure 7-b for the 4 sccm case, a large contribution to the low  $\eta_d$  comes from the development of the hollow plume structure which is thought to depend on where the MW power is deposited and on the propellant injection.

As a result of the assumptions introduced in the estimation of the partial efficiencies, a discrepancy arises when comparing the thrust and thrust efficiency obtained with the TB with the one resulting from the indirect measurements (equation 9). Section III E analyzes the main sources for this difference by comparing the direct and indirect thrust. Nevertheless, the product of the partial efficiencies presented here as in equation 9 can provide a qualitative interpretation for the different trends seen in  $\eta_F$  (refer to figure 3-c). This product is shown in figure 7-d.  $\eta_F$  for the 2 sccm case was shown to decrease with power, this trend is ascribed to the drop in  $\eta_e$ , since  $\eta_d$  and  $\eta_u$  stay rather constant. On the other hand, for the 4 sccm case, the transition from the hollow to single peak plume and the increasing utilization are enough to compensate for the slower decrease in energy efficiency, leading to a global increase of thrust efficiency with power. Lastly, at 8 sccm, the notable increase in  $\eta_u$  should logically result in a corresponding rise in  $\eta_F$ , given that  $\eta_d$  and  $\eta_e$  remain relatively constant. However, the absence of such a trend in figure 3-c may suggest a more pronounced discrepancy between direct and indirect measurements for this mass flow rate.

### E. Direct vs Indirect thrust measurements

Table II and figure 8 compare the estimated ion thrust  $F_{i\infty}$ , evaluated as in equation 7, against the direct thrust measurements  $F_{TB}$ . The computed thrust is a fraction of the one measured by the TB, ranging between 43% and 86% of the latter. The thrust levels at 2 and 4 sccm show good agreement at lower power levels, but the agreement slightly reduces for the maximum power case ( $\approx 260$  W). An opposite trend is observed for the working points at 8 sccm,  $F_{i\infty}/F_{TB}$  is the lowest for this case, staying below 60%. In a similar way, in<sup>6</sup>, Vialis *et al.* found that electrostatic probe measurements were underestimating direct thrust measurements of a coaxial ECRT by about 20% and partially attributed this effect to the intrusive nature of the FC. However, in the present study, no evident change in thruster performance was observed during FC operation.

The observed discrepancy between direct and indirect ion thrust estimation may stem from other contributions to thrust that have not been taken into account. The total thrust force,  $F$ , can be written as the sum of the axial momentum brought by all the species in the plasma plume:

$$F = F'_{i\infty} + F_{e\infty} + F_n; \quad (14)$$

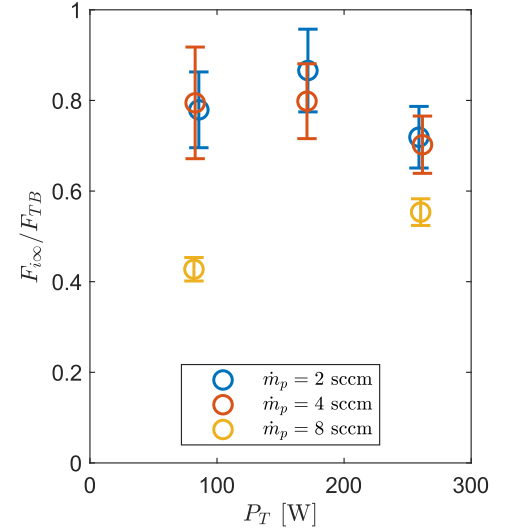


FIG. 8. Ratio between the thrust estimated with electrostatic probes  $F_{i\infty}$  (equation 7), and direct thrust measurements  $F_{TB}$ , for  $\dot{m}_p = 2 - 4 - 8$  sccm respectively in blue, red and yellow.

where  $F'_{i\infty}$  is the ion thrust including the effects of multiply-charged ions and  $F_{e\infty}$  and  $F_n$  are the thrust produced by electrons and neutrals respectively. These last two terms are generally neglected since their contribution is considered small with respect to the one of ions. However, for the case under study, this approximation may be unjustified.

Electrons have negligible inertia, hence, their main momentum contribution comes from their pressure  $p_e = nT_e$ . Assuming quasi-neutrality, a uniform electron temperature along the  $\alpha$  direction, and  $\kappa_2 = 1$ , an approximation of  $F_e$  can be given by the ratio of momentum fluxes of electrons and ions:

$$F_e \simeq F_i \frac{nT_e}{nm_i u_i^2} = \frac{F_i}{M_i^2}. \quad (15)$$

where  $M_i$  is the ion Mach number. The latter can be evaluated by combining the results from the Langmuir probe and RPA measurements. However, we are interested in knowing  $F_{e\infty}$  which requires the knowledge of  $T_{e\infty}$ . In the case of an experiment performed within a vacuum chamber, an expansion to infinity is not possible and a sheath will develop at the vacuum chamber walls where  $\phi = 0$  V. Since, the electron temperature and density there are not zero, electrons may still provide a residual pressure. The electron temperature in the vicinity of the wall is not known, however, an upper bound to the momentum contribution of the electrons is provided by the  $T_e$  measurements at  $\rho = 350$  mm, corresponding to the assumption of an isothermal expansion from there up to the walls. As an example, for the case at 2 sccm and  $P_T \approx 175$  W, the electron temperature at  $\rho = 350$  mm resulted to be  $T_e = 11.5$  eV and the ion velocity  $u_{i\infty} \approx 13$  km/s, leading to  $F_{e\infty}/F_{i\infty} \approx 1/M_{i\infty}^2 = 4.6\%$ . In reality, this value is expected to be lower both because of the electron cooling along the magnetic nozzle plume expansion and because of the break-

$\dot{m}_p$ [sccm]	2			4			8	
$P_T$ [W]	80	175	260	80	175	260	80	260
$I_i$ [A]	0.067	0.073	0.076	0.090	0.122	0.128	0.106	0.198
$I_{zi}$ [A]	0.052	0.056	0.058	0.063	0.089	0.096	0.073	0.138
$\eta_u$ [%]	47	51	53	31	43	45	18	35
$\eta_d$ [%]	59	59	58	49	54	56	48	49
$\eta_e$ [%]	6.4	5.3	3.9	5.5	4.7	4.2	3.9	3.9
$\eta_s$ [%]	99	99	97	99	99	99	99	99
$F_{i\infty}$ [mN]	0.76	1.03	1.08	0.74	1.19	1.46	0.66	1.62
$F_{e\infty}$ [mN]	<0.04	<0.05	–	<0.02	–	–	–	–
$F_n$ [mN]	0.04	0.04	0.04	0.1	0.09	0.08	0.2	0.2
$F_{TB}$ [mN]	0.98	1.19	1.51	0.93	1.49	2.08	1.55	2.96

TABLE II. Table summarizing the data presented in section III D and section III E.  $I_i$  and  $I_{zi}$  are the integral ion currents as defined in equations (5) and (6).  $\eta_u$ ,  $\eta_d$ ,  $\eta_e$ ,  $\eta_s$  are the utilization, divergence, energy, and dispersion efficiencies as defined in equations (10)–(13).  $F_{i\infty}$  and  $F_{e\infty}$  are the ion and electron thrust contributions, following equations (7) and (15).  $F_n$  is the neutral thrust contribution from equation (16) for  $T_n/T_n^0 = 3$ . The direct thrust measurement  $F_{TB}$  is included in the next row for comparison.

ing of quasi-neutrality within the sheath at the vacuum chamber walls, as the electron density is reduced with respect to the one of the ions.

Concerning the contribution of neutrals,  $F_n$ , we first introduce the cold gas thrust,  $F_n^0$ , defined as the force measured by the TB when only propellant but no MW power is injected (no plasma).  $F_n^0$  is linear with the propellant flow rate as depicted in figure 9-a. After the thruster ignition, the flow of neutrals is reduced by ionization and can be approached as  $\dot{m}_n = \dot{m}_p(1 - \eta_u)$ . Conversely, their temperature  $T_n^0 \rightarrow T_n$  increases thanks to the higher wall temperature, plasma-wall recombination generating energetic neutrals, and charge-exchange collisions<sup>36,37</sup>. For any non-reacting neutral gas expanding into vacuum,  $F_n \propto \dot{m}_n \sqrt{T_n}$ , so

$$F_n \simeq F_n^0 (1 - \eta_u) \sqrt{\frac{T_n}{T_n^0}}, \quad (16)$$

with  $F_n$  and  $T_n$  referring to plasma-on conditions. Obviously, the importance of the neutrals' contribution to thrust increases with  $T_n$  and decreases with  $\eta_u$ . Using the  $\eta_u$  estimations from figure 7-a, the role of  $T_n$  is illustrated in Figure 9-b. The value of  $T_n$  is unknown and it is expected to vary with the thruster operating point, however, values between 800-900 K are realistic in ECR sources and magnetic nozzles thrusters<sup>36–38</sup>. This points out that at 8 sccm (80 W), which is the case with the lowest utilization efficiency, neutral thrust could be worth up to 16% of the total thrust under the assumption of  $T_n/T_n^0 = 3$ , while this would be only 10% if neutral gas does not experience any heating after thruster ignition ( $T_n = T_n^0$ ). On the other hand, for the case at  $\dot{m}_p = 2$  sccm and 80 W, which presents a much higher utilization, neutral thrust contribution would remain close to 4%. Thus, without invoking unrealistically high neutral heating, neutrals can only compensate partially for the discrepancy; furthermore, their contribution becomes relevant only for the low  $\eta_u$  cases.

In the previous sections, we have assumed the presence of singly charged ions only. However, multiple ionization might occur in the discharge chamber due to the relatively high elec-

tron temperature and plasma density available in this kind of device<sup>15</sup>. Referring to equation 6, the total axial current can be written as:  $I_{zi} = I_{zi1} \sum_j R_j$ , where  $j$  indicates the ion species and  $R_j = I_{zij}/I_{zi1}$ . An ExB probe would be necessary in order to experimentally measure the proportion and velocities of the different ion species. However, assuming these ions are subject to the same electric potential difference as singly-charged ones and that the velocity dispersion  $\kappa_2$  does not vary for each species, a correction to the ion thrust can be written as:

$$F'_{i\infty} = F_{i\infty} \frac{\sum_j R_j / \sqrt{Z_j}}{\sum_j R_j} = F_{i\infty} \alpha_F \quad (17)$$

where  $Z_j$  is the ion charge number. In<sup>22</sup>, the double-to-single ion production ratio in the source was estimated using  $v_{n \rightarrow i2}/v_{n \rightarrow i1}$ , where  $v$  is the electron collision frequency,  $n$  stands for neutrals and  $i1$ ,  $i2$  for singly and doubly charged Xe ions respectively. This value depends on  $T_e$ , which in turn is expected to increase with  $P_T$  and reduce with  $\dot{m}_p$ . Following the same procedure as in<sup>22</sup>, we estimate  $v_{n \rightarrow i2}/v_{n \rightarrow i1} \approx 5.5\%$  for 2 sccm and 260 W (case with the highest  $P_T/\dot{m}_p$  in this study), where a  $T_e = 15$  eV was measured at  $z = 150$  mm, and a lower fraction for all other cases. Hence, considering the presence of doubly-charged ions only, the thrust  $F_{i\infty}$  should be corrected with a factor of  $\alpha_F \approx 0.97$ . This correction reduces the estimation of the measured indirect ion thrust, and therefore it cannot justify the thrust difference between direct and indirect measurements. Note that this correction due to double ions is not reflected in the data of table II. On a side note, the possible presence of multiply charged ions would also affect the  $\eta_u$  estimation and thus  $F_n$  (refer to equation 16). Using the above-provided values,  $\eta_u$  might be overestimated by up to 5.2%, computed according to<sup>39</sup>.

These estimations imply that other sources of disagreement may lie in the assumptions taken. One of these may be neglecting the effects of the high-energy electrons on the ion current density measurements with the FC, as discussed in section III C. Indeed, a fraction of these electrons were found to have energies that exceeded the typical FC collector bias. If



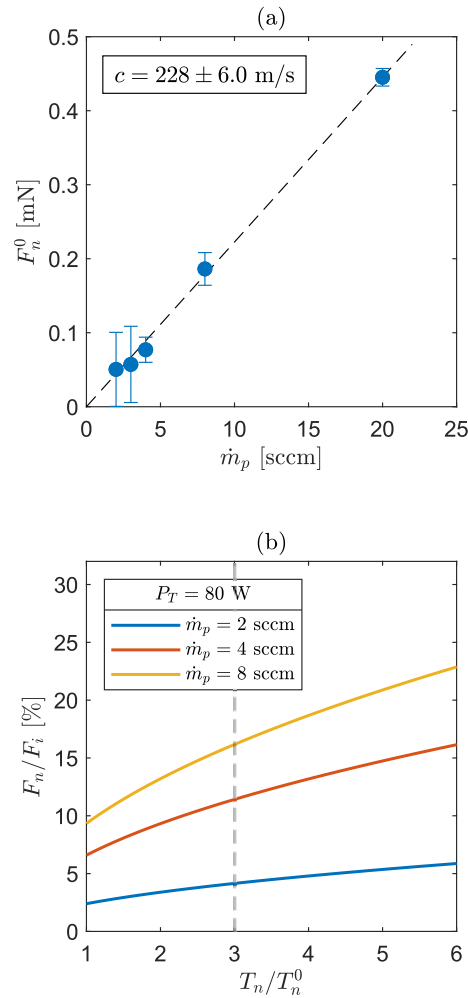


FIG. 9. (a) Direct thrust measurements of cold Xenon propellant gas (temperature  $T_n^0$ ) ejected from the thruster at different mass flow rates. (b) The expected contribution of the neutral thrust to the total thrust as a function of the temperature ratio  $T_n/T_n^0$ .

these electrons are not only present on the axis, then it would result in an underestimation of the utilization efficiency. This phenomenon may be responsible for the decrease of  $F_{i\infty}/F_{TB}$  at 260 W for 2 and 4 sccm, but not for the 8 sccm case for which they were not observed. Hence, the reasons for the larger discrepancy at this mass flow rate are still unknown, and further investigation is warranted. It is reasonable to speculate that the thrust discrepancy may be partly due to an underestimation of the ion current density  $j_i$  measured by the FC. Charge exchange collisions in the far plume may cause such a phenomenon by producing both, fast neutrals and slow ions. The firsts are not detectable by an FC and little energy is lost in these collisions<sup>40</sup>, whereas the probability of collection of a slow ion is reduced. This effect would result in an increased discrepancy between TB and indirect measurements, partic-

ularly for large mass flow rates due to the increased back-ground pressure. A possible parallel effect contributing to the reduced measured current could be the effective FC aperture being smaller than the geometrical probe aperture (see section II): e.g. a  $\approx 10\%$  smaller effective FC aperture diameter relative to the geometrical one,  $D_{FC}$ , is enough to explain a 20% underestimation of  $I_i$ . This effect may be more pronounced for slower ions, such as those at 8 sccm, which could explain the larger discrepancy in that case.

#### IV. CONCLUSION

Direct thrust and electrostatic probe measurements of a waveguide ECR thruster prototype have been presented and discussed. The prototype is able to produce up to 3.5 mN of thrust at 8 sccm and 350 W of input MW power (with  $\eta_F = 2.1\%$ ). Thrust has been shown to present linear trends with power at fixed  $\dot{m}_p$ . At a lower mass flow rate, the thrust is reduced and the thrust efficiency is increased. A maximum thrust efficiency of  $\eta_F = 3.5\%$  was measured for 2 sccm and 61 W (with  $F_{TB} = 0.9$  mN), this value is in line with the low thrust efficiency measured in other similar devices. Electrostatic probe measurements allowed the identification of the loss mechanisms resulting in this low  $\eta_F$ . This was done by decomposing the latter into partial efficiencies.

The most constraining factor has been shown to be energy efficiency, staying below 7% for all the cases studied, meaning that the greatest part of the input power is either lost to the walls or in inefficient plasma production, instead of axial beam power. The utilization efficiency  $\eta_u$  scales roughly with  $P_T/\dot{m}_p$ , and reaches a maximum of  $\eta_u \approx 50\%$  being the second highest source of loss. This waveguide ECRT prototype also showed a high plume divergence. The divergence efficiency  $\eta_d$  is particularly low for the cases with low  $P_T/\dot{m}_p$  since the plume becomes hollow at these operating points, a behavior which could be possibly linked to the neutral gas radial injection driving power absorption in proximity to the walls. Efforts to simulate the propagation and absorption of microwave power within the PC with numerical models are expected to further provide clues on these phenomena and will be the subject of future works. We suggest that an improved injector strategy, such as an axial injection, may help eliminate/reduce power coupling to higher radii, possibly also having repercussions on the utilization and divergence efficiency.

The RPA-IEDF measurements provided insights into additional phenomena: an increased dispersion of ion velocity with increasing power, suggesting an enlargement of the ionization region scaling with  $P_T$  and the presence of an energetic electron tail in the plume up to 300 eV. Further research is needed to understand the origins of these electrons and their effects on discharge physics since it could pave the way for enhanced performance in future thruster designs.

The plume measurements allowed for the indirect assessment of thrust. A discrepancy between the direct and indirect estimations was found. Estimates of thrust from other species suggest that hot neutrals could contribute significantly to the total thrust, but they are not enough to fully explain the

data. The thrust contribution by multiply charged ions and electrons was also evaluated, however, their effect is considered marginal. Assuming that TB measurements are accurate within the provided accuracy range, it is suggested that FC ion current measurements could be a potential source of thrust discrepancy. The presence of energetic electrons, charge exchange collisions, and an overestimation of the Faraday Cup's effective aperture may contribute to an underestimation of the beam current. Future tests will aim to corroborate these hypotheses. The effect of charge exchange collisions on the thrust discrepancy may be investigated by varying the vacuum chamber pressure. On the other hand, iterations on probe geometries may help reduce the error on the FC effective collection area and enable the use of larger collector biases to repel energetic electrons.

## ACKNOWLEDGMENTS

This work has been supported by the R&D project PID2019-108034RB-I00 (ESPEOS), funded by MCIN/AEI/10.13039/501100011033. The contribution of M. Merino has been supported by the funding from the European Research Council (ERC) under the European Union's Horizon 2020 research and innovation program, project ZARATHUSTRA, grant agreement No 950466.

## CONFLICT OF INTEREST

The authors have no conflicts to disclose.

## DATA AVAILABILITY

The data that support the findings of this study are available from the corresponding author upon reasonable request.

## Appendix A: Thrust Balance calibration system and thrust measurement procedure

This section describes the new calibration system employed for the thrust balance described in<sup>25</sup>. The use of calibrated masses for thrust balance calibration is an accurate, repeatable, and reliable means to obtain the displacement/force relation characteristic of the thrust balance assembly. Systems such as the ones described in<sup>26,41,42</sup> all rely on the use of calibrated masses (typically fishing weights) loaded on a wire. In those systems, their weights directly apply an equivalent thrust force on the pendulum by using a pulley; However, systems of that kind are subject to friction between the pulley and the wire, which must be taken into account for a precise measurement<sup>41</sup>.

The system here described uses an additional calibration arm, perpendicular to the pendulum axis of length  $L_{cal} = 170$  mm, the masses apply their weights on the arm, hence a torque is applied on the pendulum without the need for a pulley. A

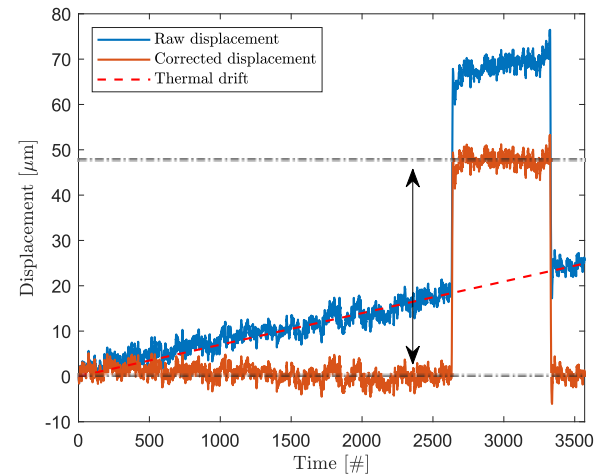


FIG. 10. Example of thrust measurement. The water cooling system was on during this measurement.

schematic representation of the new calibration system is presented in figure 11-a. The calibrated weights have a mass of  $m_{cal} \approx 0.5$  gr. A precise measurement of their mass is obtained with a mass balance (Shimadzu AUW220D) with an accuracy in the mg range. These masses are loaded on a thin nylon wire ( $\varnothing = 0.16$  mm) separated by a distance of 25 mm, one end of the wire is attached to the calibration arm, while the other side is wrapped around a spool driven by a stepper motor. The reference for the spool angular position is provided by a limit switch which is pushed by a mechanical pin mounted on a second disk. The latter and the pulley are both 3D printed and equipped with gears. The gear ratio between them is 5, allowing up to five full rotations of the spool. A CAD representation of the assembly is provided in figure 11-b. As the spool is rotated, the masses are lowered and their weight is applied one by one on the calibration arm. This creates a torque on the TB that is recorded as displacement by the displacement sensor. The displacement provided is equivalent to the one given by a thrust force  $F_{req} = F_{cal}L_{cal}/L_t$ , where  $L_t$  is the thrust vector distance from the vertical arm pivot point. The latter has been measured to be  $L_t = 686.5$  mm. In order to keep the wire constantly under tension, at least one weight is always applied on both of its sides. In this work, between 3 and 5 weights are applied in total during the calibration procedure. A typical calibration output displacement is shown in figure 12. For this particular case, the calibration factor  $k_{cal}$  found for the balance is  $k_{cal} = 66.88$  mN/mm with a relative uncertainty of 0.044%. Once  $k_{cal}$  is obtained, the thrust  $F_{TB}$  is simply obtained with

$$F_{TB} = \frac{L_{cal}}{L_t} k_{cal} y = \kappa_s y, \quad (A1)$$

where  $y$  is the displacement due to the thrust force and  $\kappa_s$  is the equivalent stiffness of the balance.

Although the TB is equipped with a cooling system, thermal loads affect the position of the pendulum+thruster barycenter leading to TB displacement to drift with time.

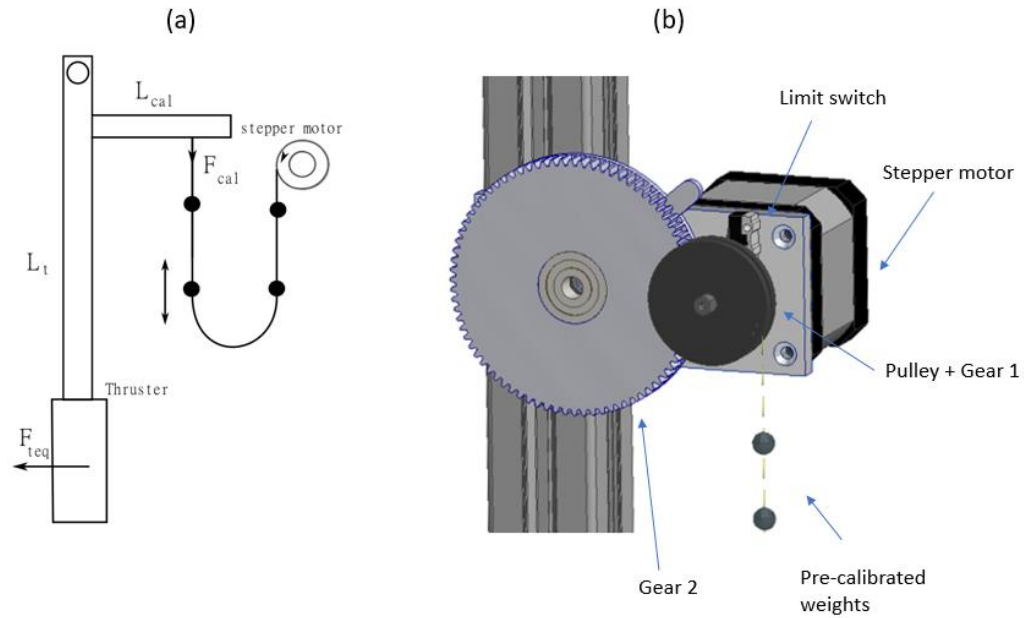


FIG. 11. (a) Schematic representation of the weights calibration system. (b) CAD view of the weight calibration system.

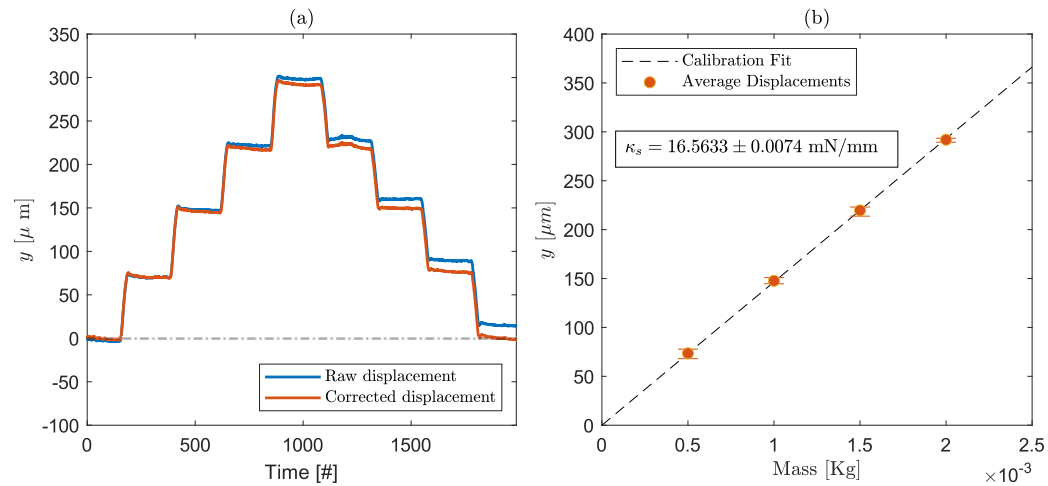


FIG. 12. (a) Typical calibration output displacement. (b) Calibration curve resulting from the post-processing of the displacement in panel-a.

Thus, calibrations are performed before and in between thrust measurements to correct for this drift.

Thrust measurements are performed as follows: the desired  $\dot{m}_p$  is set on the mass flow controller, the input power is set on the MW generator to obtain the thruster ignition, the thruster is ignited and left on for the time necessary to reach the steady state, condition monitored using  $V_T$  and  $\Gamma_L^2$ . Then the power and the mass flow are cut. The reference for the TB displacement is thus taken. An example of thrust measurement is shown in figure 10. A similar procedure is carried out for performing the neutral thrust measurements shown in figure 9-a, however for this case, no microwave power is provided as input.



- <sup>1</sup>S. Bathgate, M. Bilek, and D. McKenzie, "Electrodeless plasma thrusters for spacecraft: a review," *Plasma Science and Technology* **19**, 083001 (2017).
- <sup>2</sup>K. Takahashi, "Helicon-type radiofrequency plasma thrusters and magnetic plasma nozzles," *Reviews of Modern Plasma Physics* **3**, 3 (2019).
- <sup>3</sup>G. Crimi, A. Eckert, and D. Miller, "Microwave driven magnetic plasma accelerator studies (cyclops)," *Tech. Rep.* (General Electric Company, Space Sciences Laboratory, Missile and Space Division, 1967).
- <sup>4</sup>J. Sercel, *An experimental and theoretical study of the ECR plasma engine*, Ph.D. thesis, California Institute of Technology (1993).
- <sup>5</sup>F. Cannat, T. Lafleur, J. Jarrige, P. Chabert, P. Elias, and D. Packan, "Optimization of a coaxial electron cyclotron resonance plasma thruster with an analytical model," *Physics of Plasmas* **22**, 053503 (2015).
- <sup>6</sup>T. Vialis, J. Jarrige, A. Aanesland, and D. Packan, "Direct thrust measurement of an electron cyclotron resonance plasma thruster," *Journal of Propulsion and Power* **34**, 1323–1333 (2018).
- <sup>7</sup>S. Peterschmitt and D. Packan, "Impact of the microwave coupling structure on an electron-cyclotron resonance thruster," *Journal of Propulsion and Power* **37**, 806–815 (2021).
- <sup>8</sup>V. Désangles, D. Packan, J. Jarrige, S. Peterschmitt, P. Dietz, S. Scharmann, K. Holste, and P. J. Klar, "Ecra thruster advances: 30w and 200w prototypes latest performances," *Journal of Electric Propulsion* **2**, 10 (2023).
- <sup>9</sup>T. H. Stix, *Waves in plasmas* (Springer Science & Business Media, 1992).
- <sup>10</sup>J. Bittencourt, *Fundamentals of plasma physics* (Springer, Berlin, Germany, 2004).
- <sup>11</sup>E. Ahedo and M. Merino, "Two-dimensional supersonic plasma acceleration in a magnetic nozzle," *Physics of Plasmas* **17**, 073501 (2010).
- <sup>12</sup>M. Merino and E. Ahedo, "Magnetic nozzles for space plasma thrusters," in *Encyclopedia of Plasma Technology*, Vol. 2, edited by J. L. Shohet (Taylor and Francis, 2016) pp. 1329–1351.
- <sup>13</sup>J. Zhou, A. Domínguez-Vázquez, P. Fajardo, and E. Ahedo, "Magnetized fluid electron model within a two-dimensional hybrid simulation code for electrodeless plasma thrusters," *Plasma Sources Science and Technology* **31**, 045021 (2022).
- <sup>14</sup>P. Jiménez, J. Zhou, J. Navarro-Cavallé, P. Fajardo, M. Merino, and E. Ahedo, "Analysis of a cusped helicon plasma thruster discharge," *Plasma Sources Science and Technology* (2023), 10.1088/1361-6595/ad01da.
- <sup>15</sup>A. J. Sheppard and J. M. Little, "Performance analysis of an electron cyclotron resonance thruster with various propellants," *Journal of Propulsion and Power*, 1–11 (2022).
- <sup>16</sup>B. N. Wachs and B. A. Jorns, "Sub-millineutron thrust stand and wireless power coupler for microwave-powered small satellite thrusters," *Review of Scientific Instruments* **93** (2022).
- <sup>17</sup>D. B. Miller and E. F. Gibbons, "Experiments with an electron cyclotron resonance plasma accelerator," *AIAA Journal* **2**, 35–41 (1964).
- <sup>18</sup>D. Miller, E. Gibbons, and P. Gloersen, "Cyclotron resonance propulsion system," in *Electric Propulsion Conference* (1962) p. 2.
- <sup>19</sup>E. Ahedo and M. Martínez-Sánchez, "Theory of a stationary current-free double layer in a collisionless plasma," *Physical Review Letters* **103**, 135002 (2009).
- <sup>20</sup>M. R. Inchingolo, M. Merino, and J. Navarro-Cavallé, "Hybrid pic-fluid simulation of a waveguide ecr magnetic nozzle plasma thruster," in *Space Propulsion Conference 2021*, 00192 (Association Aéronautique et Astronautique de France, March 17-19, 2021).
- <sup>21</sup>M. Inchingolo, J. Navarro-Cavallé, and M. Merino, "Design and plume characterization of a low-power circular waveguide coupled ecr thruster," in *5<sup>th</sup> International Workshop on Micropropulsion and CubeSats* (Toulouse (online), 2021).
- <sup>22</sup>M. R. Inchingolo, M. Merino, and J. Navarro-Cavallé, "Plume characterization of a waveguide ecr thruster," *Journal of Applied Physics* **133**, 113304 (2023).
- <sup>23</sup>A. E. Vinci, M. R. Inchingolo, S. Mazouffre, and J. Navarro-Cavallé, "Ion dynamics in the magnetic nozzle of a waveguide ecr thruster via laser-induced fluorescence spectroscopy," *Journal of Physics D: Applied Physics* **56**, 025204 (2022).
- <sup>24</sup>D. M. Pozar, *Microwave engineering* (John Wiley & sons, 2011).
- <sup>25</sup>M. Wijnen, J. Navarro-Cavallé, and P. Fajardo, "Mechanically amplified milli-newton thrust balance for direct thrust measurements of electric thrusters for space propulsion," *IEEE Transactions on Instrumentation and Measurement* **70**, 3505318 (2021).
- <sup>26</sup>K. A. Polzin, T. E. Markusic, B. J. Stanojev, A. DeHoyos, and B. Spaun, "Thrust stand for electric propulsion performance evaluation," *Review of Scientific Instruments* **77**, 105108 (2006).
- <sup>27</sup>M. Wijnen, *Diagnostic Methods for the Characterization of a Helicon Plasma Thruster*, Ph.D. thesis, Universidad Carlos III de Madrid, Leganés, Spain (2022).
- <sup>28</sup>A. Sánchez-Villar, J. Zhou, M. Merino, and E. Ahedo, "Coupled plasma transport and electromagnetic wave simulation of an ECR thruster," *Plasma Sources Science and Technology* **30**, 045005 (2021).
- <sup>29</sup>I. H. Hutchinson, "Principles of plasma diagnostics," *Plasma Physics and Controlled Fusion* **44**, 2603 (2002).
- <sup>30</sup>F. Cichocki, J. Navarro-Cavallé, A. Modesti, and G. Ramírez Vázquez, "Magnetic nozzle and rpa simulations vs. experiments for a helicon plasma thruster plume," *Frontiers in Physics* **10** (2022), 10.3389/fphy.2022.876684.
- <sup>31</sup>E. Ahedo and M. Martínez Sánchez, "Theory of a Stationary Current-Free Double Layer in a Collisionless Plasma," *Physical Review Letters* **103**, 1–4 (2009).
- <sup>32</sup>M. Merino and E. Ahedo, "Two-dimensional quasi-double-layers in two-electron-temperature, current-free plasmas," *Physics of Plasmas* **20**, 023502 (2013).
- <sup>33</sup>C. Charles and R. Boswell, "Current-free double-layer formation in a high-density helicon discharge," *Applied Physics Letters* **82**, 1356–1358 (2003).
- <sup>34</sup>D. Berisford, R. D. Bengtson, and L. L. Raja, "Power balance and wall erosion measurements in a helicon plasma," *Physics of Plasmas* **17**, 033503 (2010).
- <sup>35</sup>P. Jiménez, L. Chacón, and M. Merino, "An implicit, conservative electrostatic particle-in-cell algorithm for paraxial magnetic nozzles," Submitted to: *Journal of Computational Physics* (2023), arXiv:2305.07146.
- <sup>36</sup>J. Hopwood and J. Asmussen, "Neutral gas temperatures in a multipolar electron cyclotron resonance plasma," *Applied physics letters* **58**, 2473–2475 (1991).
- <sup>37</sup>A. E. Vinci, S. Mazouffre, V. Gómez, P. Fajardo, and J. Navarro-Cavallé, "Laser-induced fluorescence spectroscopy on xenon atoms and ions in the magnetic nozzle of a helicon plasma thruster," *Plasma Sources Science and Technology* **31**, 095007 (2022).
- <sup>38</sup>T. Nakano, N. Sadeghi, and R. A. Gottscho, "Ion and neutral temperatures in electron cyclotron resonance plasma reactors," *Applied physics letters* **58**, 458–460 (1991).
- <sup>39</sup>D. Goebel and I. Katz, *Fundamentals of Electric Propulsion: Ion and Hall Thrusters* (Jet Propulsion Laboratory, Pasadena, CA, 2008).
- <sup>40</sup>B. Wachs and B. Jorns, "Background pressure effects on ion dynamics in a low-power magnetic nozzle thruster," *Plasma Sources Science and Technology* **29**, 045002 (2020).
- <sup>41</sup>B. R. Tartler, *Construction and performance of an inverted pendulum thrust balance*, Ph.D. thesis, Massachusetts Institute of Technology (2010).
- <sup>42</sup>A. Neumann, J. Simon, and J. Schmidt, "Thrust measurement and thrust balance development at dlr's electric propulsion test facility," *EPJ Techniques and Instrumentation* **8**, 17 (2021).